Facile synthesis of metal oxide/reduced graphene oxide hybrids with high lithium storage capacity and stable cyclability

Yan, Qingyu; Lou, David Xiong Wen; Chen, Xiaodong; Zhang, Hua; Hng, Huey Hoon; Zhu, Jixin; Zhu, Ting; Zhou, Xiaozhu; Zhang, Yanyan

2011

Zhu, J., Zhu, T., Zhou, X., Zhang, Y., Lou, D. X. W., Chen, X., et al. (2011). Facile synthesis of metal oxide/reduced graphene oxide hybrids with high lithium storage capacity and stable cyclability. Nanoscale, 3, 1084-1089.

https://hdl.handle.net/10356/106631

https://doi.org/10.1039/C0NR00744G

Nanoscale

Dynamic Article Links

Cite this: DOI: 10.1039/c0xx00000x

www.rsc.org/xxxxxx

ARTICLE TYPE

Facile synthesis of metal oxide/reduced graphene oxide hybrids with high lithium storage capacity and stable cyclability†

Jixin Zhu,[a] Ting Zhu,[b] Xiaozhu Zhou,[a] Yanyan Zhang,[a] Xiong Wen Lou,[b] Xiaodong Chen,[a] Hua Zhang,[a] Huey Hoon Hng[a] and Qingyu Yan*[ac]

Received (in XXX, XXX) Xth XXXXXXXXX 20XX, Accepted Xth XXXXXXXXX 20XX
DOI: 10.1039/b000000x

We report an environment-friendly approach to synthesize transition metal oxide nanoparticles (NPs)/reduced graphene oxide (rGO) sheets hybrids by combining the reduction of graphene oxide (GO) with the growth of metal oxide NPs in one step. Either Fe_2O_3 or CoO NPs were grown onto rGO sheets in ethanol solution through a solvothermal process, during which GOs were reduced to rGO without the addition of any strong reducing agent, *e.g.* hydrazine, or requiring any post-high-temperature annealing process. The GO or rGO during the precipitation of metal oxide NPs may act as heterogeneous nucleation seeds to facilitate the formation of small crystal grains. This may allow more efficient diffusion of Li ions and lead to high specific capacities. These metal oxide NPs–rGO hybrids were used as anodes for Li-ion batteries, which showed high capacities and excellent charge–discharge cycling stability in the voltage window between 0.01 and 3.0 V. For example, Fe_2O_3 NPs/rGO hybrids showed specific capacity of 881 mA h g^{-1} in the 90th cycle at a discharge current density of 302 mA g^{-1} (0.3 C), while CoO NPs/rGO hybrids showed a lower capacity of 600 mA h g^{-1} in the 90th cycle at a discharge current density of 215 mA g^{-1} (0.3 C). These nanohybrids also show excellent capacities at high C rate currents, *e.g.* 611 mA h g^{-1} for Fe_2O_3/rGO sample in the 300th cycle at 2014 mA g^{-1} (2 C). Such synthesis technique can be a promising route to produce advanced electrode materials for Li-ion batteries.

Introduction

Transition metal oxides (MOs) have been widely investigated as promising anode materials for high energy density lithium-ion batteries. These MO (M = Fe, Co, Ni, or Cu) electrodes have shown higher theoretical Li-ion storage capacities (>600 mA h g^{-1}) than that of conventional graphite anodes (372 mA h g^{-1}).[1–4] Moreover, due to their low cost, low toxicity and widespread availability, the MO electrodes have attracted increasing attention. However, these materials suffer from poor capacity retention due to the pulverization process.[5–8] Although improvements have been reported on the cyclability and specific capacity through nanostructuring the transition MOs,[9] preservation of high capacities after numerous charge–discharge cycles remains an important challenge due to the aggregation of the nanostructures and the collapse of their crystal structures during the insertion and extraction of Li ions.[5,10–13] Hybridizing the MO nanoparticles (NPs) with conducting matrixes, *e.g.* amorphous carbon shell, carbon nanotubes or graphene sheets, to form complex structures has been reported to be an effective route to overcome these problems.[14–18] Especially, due to the high electrical conductivity, high surface-to-volume ratio and ultra-thin thickness, graphene sheets have attracted great interests for hybridizing with different nanocrystals to produce nanohybrids that showed excellent cyclability and high specific capacity. For example, the Co_3O_4 anchored on graphene sheets exhibits a high reversible capacity of 800 mA h g^{-1} at a discharge current density of 50 mA g^{-1},[16] Fe_3O_4–graphene composite shows a reversible specific capacity approaching 1026 mA h g^{-1} after 30 cycles at a discharge current density of 35 mA g^{-1},[19] and a steady specific capacity of 625 mA h g^{-1} for SnO_2–graphene nanocomposite is obtained at a current density of 10 mA g^{-1} after over 100 cycles.[20]

Several approaches have been demonstrated to synthesis MO nanocrystals/graphene sheets hybrids.[16,20–22] For example, Co_3O_4/graphene composite was synthesized by pyrolysis of as-prepared $Co(OH)_2$/graphene composites. Graphene nanosheets decorated with Fe_3O_4 particles were obtained through thermal annealing of as-prepared iron hydroxide–graphene oxides at 873 K for 4 h. SnO_2/graphene hybrids can be prepared by pyrolysis of a mixture of hydrosol and reduced graphene oxide by toxic hydrazine.[20] These processes consist of mainly two steps, which

[a]*School of Materials Science and Engineering, Nanyang Technological University, 50 Nanyang Avenue, Singapore, 639798, Singapore*
[b]*School of Chemical and Biomedical Engineering, Nanyang Technological University, 70 Nanyang Drive, Singapore, 637457, Singapore*
[c]*Energy Research Institute@NTU, Nanyang Technological University, Singapore, 637459, Singapore*

† Electronic supplementary information (ESI) available: FESEM images and charge–discharge cycling performance. See DOI: 10.1039/c0nr00744g

require the reduction of graphene sheets by thermal annealing or adding toxic hydrazine[21,22] and thermal treatment of the NPs to form the proper nanocrystals. Only few reports have shown one-step growth of MO NPs/graphene sheets. The main challenge is that the dispersion of graphene oxides (GOs) in water relies on the charge stabilization in solution. The addition of metal cations in solution can affect the diffusion double layer formation and leads to agglomeration of GO, which hinders the formation of uniform MO/graphene nanohybrids. Thus, surfactants or polymers have to be added to maintain the dispersion of GO in solution, which may decrease the electrical conductivity of the samples.[23] Herein, we report the preparation of MO/reduced graphene oxide (rGO) nanohybrids in ethanol by a one-step solvothermal approach. Our results showed that Fe_2O_3 or CoO NPs were uniformly anchored onto rGO sheets, which were reduced *in situ* from GOs. The rGO/GO sheets may act as heterogeneous nucleation seeds to facilitate the formation of extremely small MO crystal grains, which can aid in the effective insertion and extraction of Li ions. The rGO sheets in the nanohybrids are highly conductive, which can maintain the electrical contact from the MO NPs to the current collectors and improve the cycling stability. Both Fe_2O_3/rGO and CoO/rGO nanohybrids showed high capacities and excellent cyclability, *e.g.* 881 mA h g^{-1} for Fe_2O_3/graphene in the 90th cycle at a discharge current of 302 mA g^{-1} (0.3 C), and 600 mA h g^{-1} for CoO/rGO in the 90th cycle at 215 mA g^{-1} (0.3 C). These nanohybrids also show high capacities at high C rate currents, *e.g.* 611 mA h g^{-1} for Fe_2O_3/rGO sample in the 300th cycle at 2014 mA g^{-1} (2 C). Such synthesis technique can be a promising route to produce advanced anode materials for Li-ion batteries.

Experimental

Synthesis of the graphite oxide

Graphite oxide was synthesized from natural graphite (SP-1) by a modified Hummer's method.[24–26] In brief, 1.5 g graphite powder was added into a mixture of 10 mL 98% H_2SO_4, 1.25 g $K_2S_2O_8$, and 1.25 g P_2O_5, and the solution was maintained at 80 °C for 4.5 h. The resulting pre-oxidized product was cleaned with water and dried in a vacuum oven at 50 °C. After it was mixed with 60 mL 98% H_2SO_4 and slowly added 7.5 g $KMnO_4$ at a temperature below 20 °C, then 125 mL H_2O was added. After 2 h, additional 200 mL H_2O and 10 mL 30% H_2O_2 were slowly added into the solution to completely react with the excess $KMnO_4$. After 10 minutes, a bright yellow solution was obtained. The resulting mixture was washed with diluted HCl aqueous (1/10 v/v) solution and H_2O. The graphite oxide was obtained after drying in a vacuum oven at 30 °C.

Synthesis of Fe_2O_3/rGO and CoO/rGO

50 mg graphite oxide was dispersed in 70 mL 99.9% ethanol by sonication to get graphene oxide (GO). Then, 0.5 mmol $FeCl_2$ and 50 μL 37% ammonia were added into the solution. The mixture was sealed into a Teflon-lined autoclave and maintained at 170 °C for 5 h. After it was cooled down to room temperature, the precipitation, *e.g.* Fe_2O_3/rGO, was collected and washed by ethanol.

50 mg graphite oxide was dispersed in 70 mL 99.9% ethanol by sonication to get graphene oxide (GO). Then, 2 mmol $Co(CH_3COO)_2 \cdot 2H_2O$ and 100 μL 37% ammonia were added into the solution. The mixture was sealed into a Teflon-lined autoclave and maintained at 170 °C for 5 h. After it was cooled down to room temperature, the precipitation, *e.g.* CoO/rGO, was collected and washed by ethanol.

Characterizations

The morphology of the samples was investigated by using a field-emission scanning electron microscopy (FESEM) system (JEOL, Model JSM-7600F), and the nanostructures of the samples were characterized by using a transmission electron microscopy (TEM) system (JEOL, Model JEM-2100) operating at 200 kV. To investigate the samples *via* TEM, a suspension of the MO/rGO nanohybrids in ethanol was drop-cast onto carbon-coated copper grids and dried under ambient condition. Crystal phases of samples were identified using a Scintag PAD-V X-ray diffractometer with Cu Kα irradiation. Raman spectra were obtained with a WITec CRM200 confocal Raman microscopy system with a laser wavelength of 488 nm and a spot size of 0.5 mm. The Si peak at 520 cm^{-1} was used as a reference to calibrate the wavenumber. Thermogravimetry analyses (TGA, Q500) were carried out in the temperature of 30 to 500 °C at a heating rate of 10 K min^{-1} in air.

Electrochemical measurements

The MO/rGO hybrids were dried at 150 °C for 30 min under Ar atmosphere. Then, 80 wt% active material (Fe_2O_3/rGO or CoO/rGO nanohybrids), 10 wt% acetylene black (Super-P), and 10 wt% polyvinylidene fluoride (PVDF) binder were mixed into *N*-methyl-2-pyrrolidinone (NMP). The obtained slurry was coated onto Cu foil disks to form working electrodes, which were then dried in vacuum at 50 °C for 12 h to remove the solvent. Electrochemical measurements were carried out on the CR2032 (3 V) coin-type cells with lithium metal as the counter/reference electrode, Celgard 2400 membrane as the separator, and electrolyte solution obtained by dissolving 1 M $LiPF_6$ into a mixture of ethylene carbonate (EC) and dimethyl carbonate (DMC) (EC/DMC, 50 : 50 w/w). The coin cells were assembled in an Ar-filled glovebox with concentrations of moisture and oxygen below 1.0 ppm. The charge/discharge tests were performed with a NEWARE battery tester at a voltage window of 0.01–3.0 V for Fe_2O_3/rGO samples and 0.05–3.0 V for CoO/rGO samples. Cyclic voltammetry (0.01–3 V, 0.5 mV s^{-1}) was performed with an electrochemical workstation (CHI 660C).

Results and discussion

The field emission scanning electron microscopy (FESEM) image (Fig. 1a) reveals the morphology of samples formed by reacting $FeCl_2$ with graphene oxides (GOs) in the one-step solvothermal process as described in the Experimental section. It clearly shows that the NPs are anchored uniformly on the surface of thin sheets. The reduction of GO is examined by Raman spectroscopy (Fig. 1b) and electrical conductivity measurements. Fig. 1b shows the increase in the intensity ratio of D band (located at 1362 cm^{-1}) and G band (located at 1601 cm^{-1}), *e.g.* I_D/I_G, which

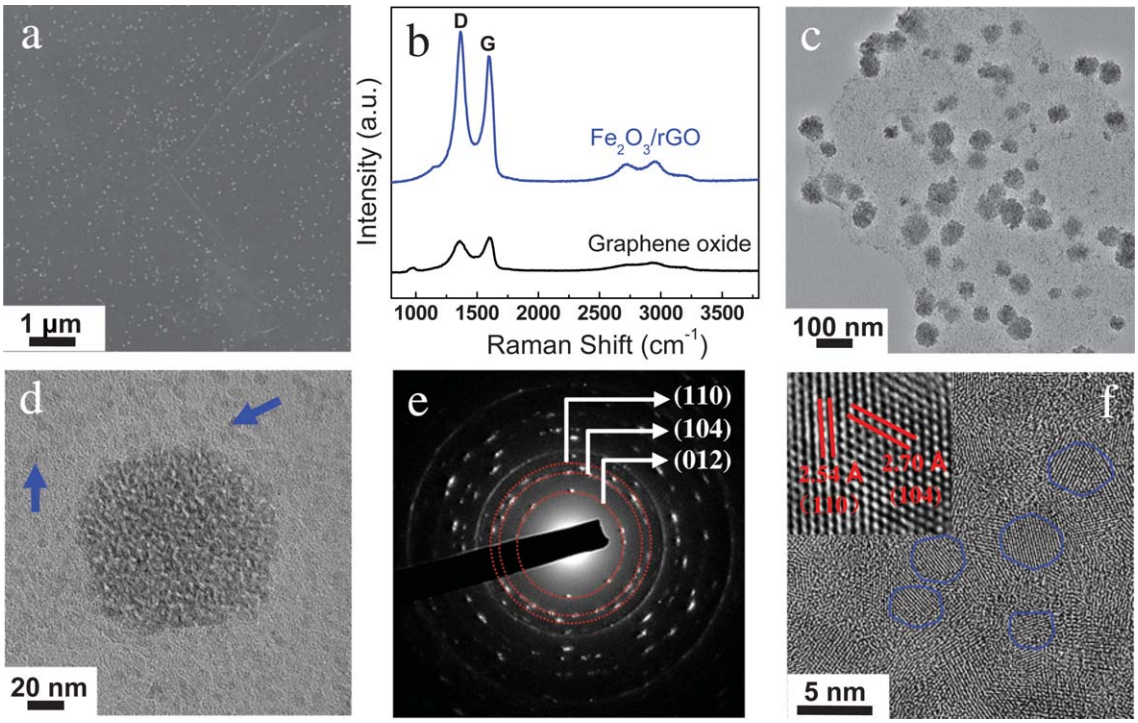

Fig. 1 (a) FESEM image of Fe_2O_3/rGO hybrid; (b) Raman spectra of the graphene oxides and Fe_2O_3/rGO hybrids; (c) Low magnification and (d) high magnification TEM image of the Fe_2O_3/rGO hybrid; the arrows in d indicate the small Fe_2O_3 nanocrystals formed on the rGO sheets; (e) SAED pattern of Fe_2O_3 NPs and (f) HRTEM image of the Fe_2O_3/rGO hybrid; the blue circuits highlight individual grains on the rGO surface.

is consistent with previous reports on GO reduction.[27,28] Meanwhile, the four-point-probe measurements show that the GO films on glass are insulating and the as-prepared samples depict a high electrical conductivity of ~250 S m^{-1}. The transmission electron microcopy (TEM) image (Fig. 1c) shows that these particles are 50–80 nm in size, while the high magnification TEM image (Fig. 1d) indicates that there are also smaller nanocrystals with size of 4–7 nm (highlighted with arrows) attached uniformly on the reduced graphene oxide (rGO). The selected area electron diffraction (SAED) pattern (Fig. 1e) of the large particles reveals ring patterns corresponding to hematite Fe_2O_3 with rhombohedral crystal structure (JCPDS89-2810), while the high resolution TEM observation (Fig. 1f) of the smaller crystals confirmed the same crystal structure. Further examination using high resolution TEM indicates the 50–80 nm Fe_2O_3 NPs are polycrystalline with grain size in range of 3–5 nm. Here, the presence of the rGO/GO sheets in the solution may act as the heterogeneous nucleation seeds to facilitate formation of such small Fe_2O_3 crystal grains, which has not been demonstrated in other process.

This similar synthetic approach is extendable to prepare other MO NPs on rGO. For example, reacting $Co(CH_3COO)_2 \cdot 2H_2O$ with GO using a similar process results in rGO decorated with NPs with size comparable to that of Fe_2O_3 (Fig. 2a), *e.g.* 40–70 nm. The Raman spectrum confirms that the GO is reduced (Fig. 2b), and the sample shows an electrical conductivity of ~200 S m^{-1} measured by four-point-probe measurement. TEM images (Fig. 2c and d) reveal that there are also small nanocrystals with size in the range of 4–7 nm on the rGO. The SAED measurement (Fig. 2e) and HRTEM observation (Fig. 2f) show that both NPs and nanocrystals are face-centered-cubic (fcc) CoO (JCPDS71-1178), where the NPs are also polycrystalline with grain size of 3–5 nm.

Fig. 3a shows the X-ray diffraction (XRD) pattern of the as-prepared MO/rGO nanohybrids, which confirms the formation of either rhombohedral Fe_2O_3 and fcc CoO phases that is consistent with the HRTEM and SAED results. No impurity phase is detected in both types of samples. A broad hump at 2θ of about 25° in XRD patterns is attributed to the glass substrate and it overlaps with the (012) peak of hematite Fe_2O_3 for the Fe_2O_3/rGO sample. We have estimated the weight ratio between MO (*e.g.* either Fe_2O_3 or CoO) and rGO, *e.g.* $I_{MO:rGO}$, by thermal gravimetric analysis (TGA) in air (see Fig. 3b). Assuming the final residues are only either Fe_2O_3 or Co_3O_4 after heating the samples to above 500 °C in air, we calculated the weight ratio to be $I_{Fe_2O_3:\,rGO} = 5.9$ and $I_{CoO:\,rGO} = 4.3$ for Fe_2O_3/rGO and CoO/rGO nanohybrids respectively. Here, in Fig. 3b, the weight loss at the temperature below 100 °C is attributed to the evaporation of moisture.

To study the Li-ion storage capabilities of both nanohybrids, a series of electrochemical measurements were carried out based on the half-cell configuration[21,22] by using the nanohybrids as the anodes. Fig. 4a depicts the representative CVs of Fe_2O_3/rGO at a scan rate of 0.5 mV s^{-1} for the first, second, and third cycles. For the first cycle curve, there are three peaks at 1.74, 1.38 and 0.73 V, respectively, which corresponds to the following three lithiation steps.[5,29]

$$\alpha\text{-}Fe_2O_3 \rightarrow \alpha\text{-}Li_xFe_2O_3 \rightarrow \text{cubic } Li_2Fe_2O_3 \leftrightarrow Fe + Li_2O$$

Fig. 4b shows the charge–discharge voltage profiles of the Fe_2O_3/rGO nanohybrid electrode for the first two cycles and the ninetieth cycle at a current rate of 302 mA g^{-1} (0.3 C, where 1 C is

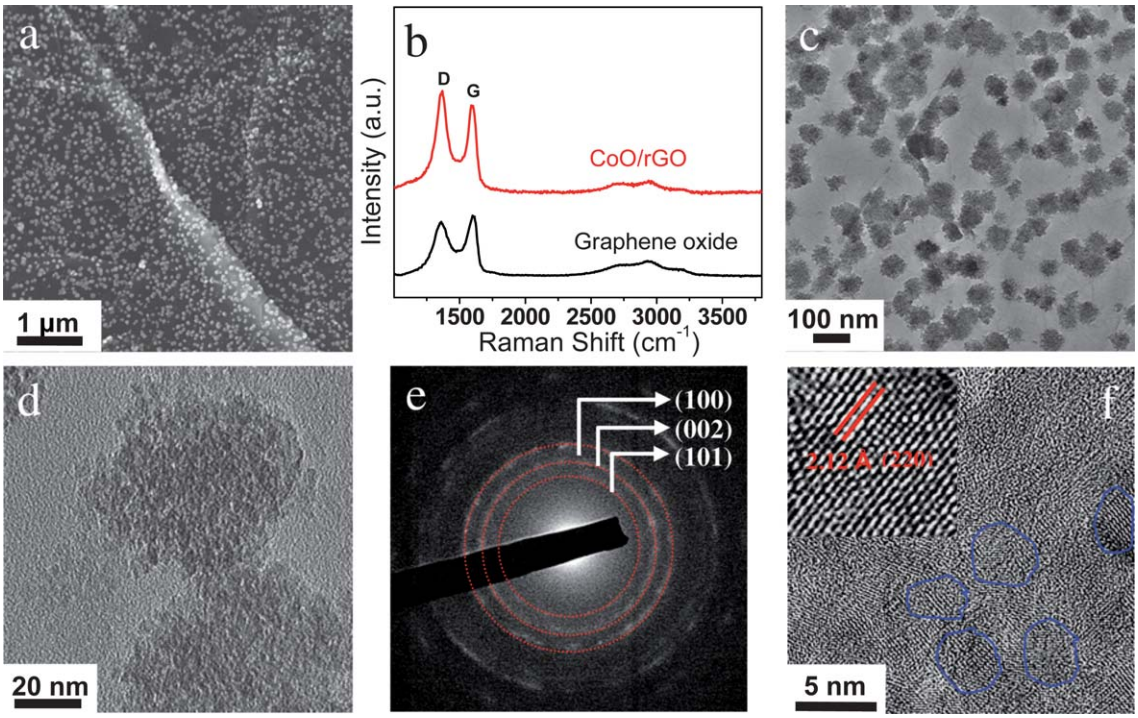

Fig. 2 (a) FESEM image of the CoO/rGO hybrid; (b) Raman spectra of graphene oxide and CoO/rGO hybrids; (c) Low magnification and (d) high magnification TEM image of the CoO/rGO hybrid; (e) SAED pattern of CoO NPs and (f) HRTEM image of the CoO/rGO hybrid; the blue circuits highlight individual grains on the rGO surface.

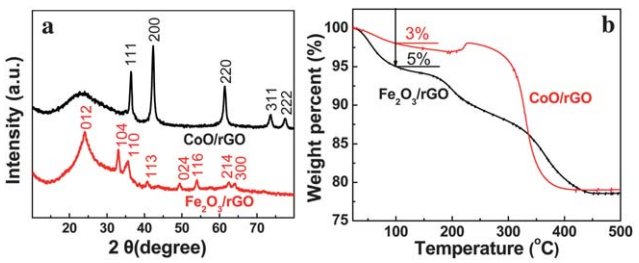

Fig. 3 (a) XRD patterns of Fe_2O_3/rGO and CoO/rGO samples. The broad hump at 25° is from the glass substrate. (b) Thermogravimetry analyses (TGA) of Fe_2O_3/rGO and CoO/rGO samples measured from 23 to 500 °C at a heating rate of 10 °C min^{-1} in air.

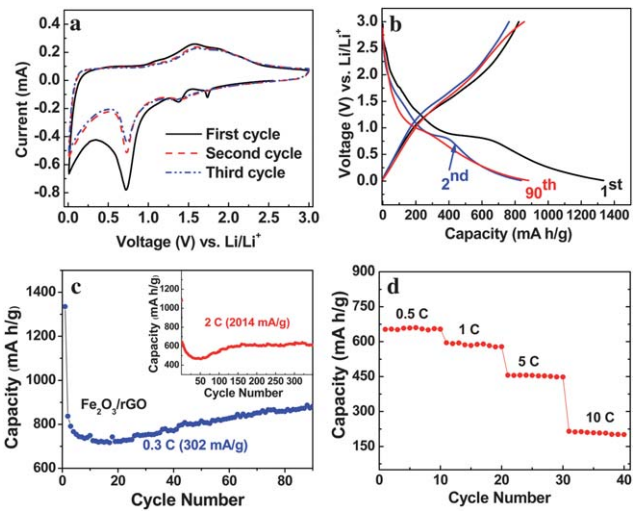

Fig. 4 (a) Representative CV curves of the Fe_2O_3/rGO hybrid electrode at a scan rate of 0.5 mV s^{-1} for the first, second, and third cycles; (b) charge–discharge voltage profiles of the Fe_2O_3/rGO electrode for the first, second and ninetieth cycles at a current density of 302 mA g^{-1} (0.3 C); (c) cycling performance of the Fe_2O_3/rGO electrode at current densities of 0.3 C and 2 C within a voltage window of 0.01–3.0 V; (d) specific capacities of the Fe_2O_3/rGO hybrid electrode for different charge/discharge cycles at various C rates. Here, 1 C is equal to 1007 mA g^{-1}.

defined as 1007 mA g^{-1}). The potential plateaus observed in the discharge curves are consistent with the CV results. The insertion process gave a first discharge capacity of 1334 mA h g^{-1} and a subsequent charge capacity of 823 mA h g^{-1}, resulting in an irreversible capacity loss of 38%. During the second cycle, the discharge capacity decreased to 837 mA h g^{-1} with a corresponding charge capacity of 764 mA h g^{-1}, leading to a much higher Coulombic efficiency of 91.3%. Moreover, the discharge and charge capacities of the hybrid improved to 881 and 856 mA h g^{-1}, respectively, in the 90th cycle, which indicates a possible activation process in the electrode material.[30] The lower capacities measured during the initial few cycles are possibly due to the trapping of the Li ions inside the Fe_2O_3 crystal framework, which are released gradually upon cycling and the capacity increases.[30] The Coulombic efficiency increased, accordingly, to 97.2%.

The discharge–charge cycling performance of the as-prepared Fe_2O_3/rGO nanohybrids was evaluated between 0.01 and 3.0 V at 0.3 C (Fig. 4c). A high discharge capacity of 837 mA h g^{-1} was delivered in the second cycle, which is ~83.1% of the theoretical

value of Fe_2O_3 (1007 mA h g^{-1}). The small grains in Fe_2O_3 NPs and the small Fe_2O_3 nanocrystals, as seen in the HRTEM results, allow the efficient diffusion of Li ions,[31] which helps to realize the high specific capacities. Although the capacity decreased slightly during the first 17 cycles to 718 mA h g^{-1}, it started to show an upward trend after the 18th cycle, which is mainly attributed to the activation process.[30] The specific capacity of the Fe_2O_3/rGO anodes reached 881 mA h g^{-1} in the 90th cycle, revealing their excellent cyclability. The Fe_2O_3/rGO anode electrodes also exhibit excellent reversible capacity and cyclability even at 2 C (2014 mA g^{-1}) rate (Fig. 4c) to deliver a discharge capacity as high as 641 mA h g^{-1} in the second cycle. The capacity slowly decreased to 470 mA h g^{-1} during the first 40 cycles and then increased to 541 mA h g^{-1} in the 100th cycles. The cycling responses of the Fe_2O_3/rGO nanohybrids at different C rates were evaluated as shown in Fig. 4d. The sample showed a capacity as high as 653 mA h g^{-1} with a current density of 0.5 C, which changed to 595 and 456 mA h g^{-1} at 1 and 5 C, respectively, though it decreased to 215 mA h g^{-1} at 10 C. Here, Fe_2O_3/rGO nanohybrids show better performances in term of Li ion storage capacity and cycling stability as compared to reported value for pure Fe_2O_3 nanoparticles,[2,5,32–34] especially at high C rate (*e.g.* 2 C). For example, Fe_2O_3 nanospheres can deliver a reasonable discharge capacity as high as 800 mA h g^{-1} in the second cycle, but it quickly fades to 414 mA h g^{-1} after 60 cycles at 100 mA g^{-1} (0.13 C) as recently reported.[5] We also prepared the Fe_2O_3 nanoparticles by similar process without addition of GOs. The size of particles is ~100 nm (see ESI, Fig. S1a†). These pure Fe_2O_3 nanoparticles delivered much lower capacities, *e.g.* 466 mA h g^{-1} during the second cycle and 84 mA h g^{-1} after 100 cycles (see ESI, Fig. S1b†) at a current density of 201 mA g^{-1} (0.2 C). The higher reversible capacity and cyclability presented above for the Fe_2O_3/rGO hybrids are promising, which benefit from the unique structure of the NPs/rGO hybrids. Normally, the pulverization process takes place due to the large volume swing generated during the Li ions insertion and extraction process that leads to the disintegration of anodes and hence a loss of electrical contacts.[35,36] Here, the rGO sheets in the hybrid samples serve as a highly conductive frame work to maintain the electrical contact from the MO NPs to the current collectors, and improve the cycling stability owing to their extremely high electrical conductivity and large surface area.[37]

Similar electrochemical tests were carried out for the CoO/rGO nanohybrids. The CV curves for the CoO/rGO hybrids at a scan rate of 0.5 mV s^{-1} for the first, second, and third cycles are shown in Fig. 5a. There are two peaks in the first cycle CV curve at 1.25 and 0.72 V, respectively, which correspond to the conversion reaction between CoO and Li ($CoO + 2Li^+ + 2e^- \rightarrow Li_2O + Co$).[38] The charge/discharge voltage profiles (Fig. 5b) at a current density of 215 mA g^{-1} (0.3 C) are consistent with the CV results. The sample delivered a first discharge capacity of 1342 mA h g^{-1} but with a large irreversible loss, *e.g.* Coulombic efficiency of only 57%, which is related to reactions of the electrolyte solution and the formation of a solid electrolyte interface layer.[39] Despite the large irreversible loss, a very high charge capacity of 900 mA h g^{-1} was still attained during the first cycle. An increased Coulombic efficiency of 93.9% was achieved in the second cycle with a discharge capacity of 931 mA h g^{-1} and a charge capacity of 874 mAh g^{-1}. The Coulombic efficiency was

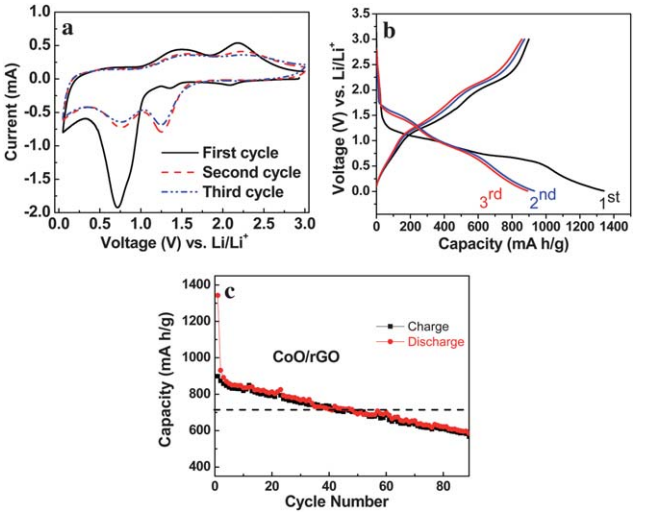

Fig. 5 (a) Representative CV curves of CoO/rGO hybrid electrodes at a scan rate of 0.5 mV s^{-1} for the first, second, and third cycles; (b) charge–discharge voltage profiles of CoO/rGO electrodes for the first, second and third cycles at a current density of 215 mA g^{-1} (0.3 C); (c) cycling performance of CoO/rGO electrodes at current densities of 215 mA g^{-1} (0.3 C) within a voltage window of 0.05–3.0 V. Here, 1 C is equal to 716 mA g^{-1}.

further increased to 96.3% in the third charge–discharge cycle, indicating a good reversibility. The CoO/rGO nanohybrids show less stable capacity retention as compared to the Fe_2O_3/rGO samples. The discharge capacity at 0.3 C rate dropped from 931 mA h g^{-1} in the 2nd cycle to 600 mA h g^{-1} in the 90th cycle (Fig. 5c). This value, however, is still much higher than that of the theoretical capacity of commercially used graphite anodes, *e.g.* 372 mA h g^{-1}. These CoO/rGO hybrids also showed better Li ion battery anode performance as compared to reported values for pure CoO.[6,40,41] For example, it was reported that[6] the CoO delivers a specific capacity of 506 mA h g^{-1} during the second cycle and then gradually decreases to 345 mA h g^{-1} at a low current density of 30 mA g^{-1}.

Conclusions

We developed an environment-friendly approach to synthesize metal oxide (MO, such as Fe_2O_3 and CoO) nanoparticles (NPs) decorated onto reduced graphene oxide (rGO) sheets to form hybrid nanostructures, which combined the precipitation of MO NPs with reduction of the graphene oxide (GO) in one step without adding any strong reducing agent, toxic hydrazine, or requiring post-high-temperature annealing. When tested as Li-ion battery anodes, these MO/rGO nanohybrids exhibited high specific capacities and excellent cyclabilities, *e.g.* in the 90th cycle, Fe_2O_3/rGO and CoO/rGO monohybrids attained 881 and 600 mA h g^{-1} at a 0.3 C rate, respectively. Such a synthetic approach can be extended to other transition metal oxides and provides promising routes to produce advanced electrode materials used for rechargeable Li-ion batteries.

Acknowledgements

The authors gratefully acknowledge AcRF Tier 1 RG 31/08 of MOE (Singapore), NRF2009EWT-CERP001-026 (Singapore)

and Singapore Ministry of Education (MOE2010-T2-1-017). H.Z. thanks the support of AcRF Tier 2 (ARC 10/10, No. MOE2010-T2-1-060) from MOE in Singapore.

References

1 X. Wang, L. J. Yu, X. L. Wu, F. L. Yuan, Y. G. Guo, Y. Ma and J. N. A. Yao, *J. Phys. Chem. C*, 2009, **113**, 15553–15558.
2 H. S. Kim, Y. Piao, S. H. Kang, T. Hyeon and Y. E. Sung, *Electrochem. Commun.*, 2010, **12**, 382–385.
3 M. Y. Cheng and B. J. Hwang, *J. Power Sources*, 2010, **195**, 4977–4983.
4 J. C. Park, J. Kim, H. Kwon and H. Song, *Adv. Mater.*, 2009, **21**, 803–809.
5 X. L. Wu, Y. G. Guo, L. J. Wan and C. W. Hu, *J. Phys. Chem. C*, 2008, **112**, 16824–16829.
6 H. Qiao, L. F. Xiao, Z. Zheng, H. W. Liu, F. L. Jia and L. Z. Zhang, *J. Power Sources*, 2008, **185**, 486–491.
7 J. Y. Xiang, J. P. Tu, L. Zhang, Y. Zhou, X. L. Wang and S. J. Shi, *Electrochim. Acta*, 2010, **55**, 1820–1824.
8 L. Yuan, Z. P. Guo, K. Konstantinov, P. Munroe and H. K. Liu, *Electrochem. Solid-State Lett.*, 2006, **9**, A524–A528.
9 C. Kim, M. Noh, M. Choi, J. Cho and B. Park, *Chem. Mater.*, 2005, **17**, 3297–3301.
10 J. Zheng, J. Liu, D. P. Lv, Q. Kuang, Z. Y. Jiang, Z. X. Xie, R. B. Huang and L. S. Zheng, *J. Solid State Chem.*, 2010, **183**, 600–605.
11 H. Xie, Y. Z. Li, S. F. Jin, J. J. Han and X. J. Zhao, *J. Phys. Chem. C*, 2010, **114**, 9706–9712.
12 G. Wang, X. P. Gao and P. W. Shen, *J. Power Sources*, 2009, **192**, 719–723.
13 L. W. Ji and X. W. Zhang, *Electrochem. Commun.*, 2009, **11**, 1146–1149.
14 J. Zhu, T. Sun, J. Chen, W. Shi, X. Zhang, X. Lou, S. Mhaisalkar, H. H. Hng, F. Boey, J. Ma and Q. Yan, *Chem. Mater.*, 2010, **22**, 5333–5339.
15 A. L. M. Reddy, M. M. Shaijumon, S. R. Gowda and P. M. Ajayan, *Nano Lett.*, 2009, **9**, 1002–1006.
16 Z. S. Wu, W. C. Ren, L. Wen, L. B. Gao, J. P. Zhao, Z. P. Chen, G. M. Zhou, F. Li and H. M. Cheng, *ACS Nano*, 2010, **4**, 3187–3194.
17 W. Wang and P. N. Kumta, *ACS Nano*, 2010, **4**, 2233–2241.
18 G. Chen, Z. Y. Wang and D. G. Xia, *Chem. Mater.*, 2008, **20**, 6951–6956.
19 G. Zhou, D.-W. Wang, F. Li, L. Zhang, N. Li, Z.-S. Wu, L. Wen, G. Q. Lu and H.-M. Cheng, *Chem. Mater.*, 2010, **22**, 5306–5313.
20 S. M. Paek, E. Yoo and I. Honma, *Nano Lett.*, 2009, **9**, 72–75.
21 D. H. Wang, R. Kou, D. Choi, Z. G. Yang, Z. M. Nie, J. Li, L. V. Saraf, D. H. Hu, J. G. Zhang, G. L. Graff, J. Liu, M. A. Pope and I. A. Aksay, *ACS Nano*, 2010, **4**, 1587–1595.
22 D. H. Wang, D. W. Choi, J. Li, Z. G. Yang, Z. M. Nie, R. Kou, D. H. Hu, C. M. Wang, L. V. Saraf, J. G. Zhang, I. A. Aksay and J. Liu, *ACS Nano*, 2009, **3**, 907–914.
23 X. Y. Qi, K. Y. Pu, X. Z. Zhou, H. Li, B. Liu, F. Boey, W. Huang and H. Zhang, *Small*, 2010, **6**, 663–669.
24 X. Z. Zhou, X. Huang, X. Y. Qi, S. X. Wu, C. Xue, F. Y. C. Boey, Q. Y. Yan, P. Chen and H. Zhang, *J. Phys. Chem. C*, 2009, **113**, 10842–10846.
25 Y. X. Xu, H. Bai, G. W. Lu, C. Li and G. Q. Shi, *J. Am. Chem. Soc.*, 2008, **130**, 5856–5857.
26 W. S. Hummers and R. E. Offeman, *J. Am. Chem. Soc.*, 1958, **80**, 1339–1339.
27 Z. J. Wang, X. Z. Zhou, J. Zhang, F. Boey and H. Zhang, *J. Phys. Chem. C*, 2009, **113**, 14071–14075.
28 S. Stankovich, D. A. Dikin, R. D. Piner, K. A. Kohlhaas, A. Kleinhammes, Y. Jia, Y. Wu, S. T. Nguyen and R. S. Ruoff, *Carbon*, 2007, **45**, 1558–1565.
29 M. V. Reddy, T. Yu, C. H. Sow, Z. X. Shen, C. T. Lim, G. V. S. Rao and B. V. R. Chowdari, *Adv. Funct. Mater.*, 2007, **17**, 2792–2799.
30 J. S. Chen and X. W. Lou, *Electrochem. Commun.*, 2009, **11**, 2332–2335.
31 J. Chen and F. Y. Cheng, *Acc. Chem. Res.*, 2009, **42**, 713–723.
32 H. Liu, G. X. Wang, J. Park, J. Wang and C. Zhang, *Electrochim. Acta*, 2009, **54**, 1733–1736.
33 B. T. Hang, H. Hayashi, S. H. Yoon, S. Okada and J. Yamaki, *J. Power Sources*, 2008, **178**, 393–401.
34 J. P. Liu, Y. Y. Li, H. J. Fan, Z. H. Zhu, J. Jiang, R. M. Ding, Y. Y. Hu and X. T. Huang, *Chem. Mater.*, 2010, **22**, 212–217.
35 Y. D. Wang, I. Djerdj, B. Smarsly and M. Antonietti, *Chem. Mater.*, 2009, **21**, 3202–3209.
36 C. H. Xu, J. Sun and L. Gao, *J. Phys. Chem. C*, 2009, **113**, 20509–20513.
37 Z. S. Wu, W. C. Ren, L. Wen, L. B. Gao, J. P. Zhao, Z. P. Chen, G. M. Zhou, F. Li and H. M. Cheng, *ACS Nano*, 2010, **4**, 3187–3194.
38 C. H. Chen, B. J. Hwang, J. S. Do, J. H. Weng, M. Venkateswarlu, M. Y. Cheng, R. Santhanam, K. Ragavendran, J. F. Lee, J. M. Chen and D. G. Liu, *Electrochem. Commun.*, 2010, **12**, 496–498.
39 D. Aurbach, Y. Eineli, B. Markovsky, A. Zaban, S. Luski, Y. Carmeli and H. Yamin, *J. Electrochem. Soc.*, 1995, **142**, 2882–2890.
40 F. Li, Q. Q. Zou and Y. Y. Xia, *J. Power Sources*, 2008, **177**, 546–552.
41 G. X. Wang, Y. Chen, K. Konstantinov, M. Lindsay, H. K. Liu and S. X. Dou, *J. Power Sources*, 2002, **109**, 142–147.